polymers

MDPI

Type of the Paper (Article)

Spatially Engraving Morphological Structure on Polymeric Surface by Ion Beam Milling

Ansu Sun [1], Ding Wang [1], Honghao Zhou [1], Yifan Li [1], Chris Connor [1], Jie Kong [3,*], Jining Sun [2,*] and Ben Bin Xu [1,*]

[1] Mechanical and Construction Engineering, Faculty of Engineering and Environment, Northumbria University, Newcastle upon Tyne, NE1 8ST, UK;
[2] School of Engineering and Physical Sciences, Heriot-Watt University, Edinburgh, UK;
[3] MOE Key Laboratory of Materials Physics and Chemistry in Extraordinary Conditions, Shaanxi Key Laboratory of Macromolecular Science and Technology, School of Science, Northwestern Polytechnic University, Xi'an, 710072, P. R. China.

* Correspondence: ben.xu@northumbria.ac.uk; jining.sun@hw.ac.uk; kongjie@nwpu.edu.cn;

Received: date; Accepted: date; Published: date

Abstract: Polymer surface patterning and modification at micro/nano scale has been discovered with great impact in applications such as microfluidics and biomedical technologies. We proposed a highly efficient fabricating method for polymer surface which had control over the surface roughness. This was achieved by polymer positive diffusion effect (PDE) for ion bombarded polymeric hybrid surface through Focused Ion Beam (FIB) technology. The PDE was theoretically analyzed by introducing positive diffusion term into the classic theory. The conductivity induced PDE constant was discussed as functions of substrates conductivity, ion energy and flux. Theoretical analysis results successfully predicted the experiential results on the conductivity-induced PDE effect on surface roughness control and patterning milling depth. Resulted micro-roughness patterns have demonstrated surface wettability control in hydrophobic and superhydrophobic surfaces (contact angles CA range from 108.3° to 150.8°) with different CA hysteresis values range from 31.4° to 8.3°.

Keywords: Ion beam milling, Topographic surface, Wetting, Contact angle hysteresis

1. Introduction

Surface patterning and modification at micro-/nano-scales have been seen of great importance in creating functional surfaces for a wide range of applications, such as water repelling and self-cleaning [1-4], antifouling [5], anti-icing [6], adhesion control and drag reduction technologies [7,8]. To create the required roughness and topography, polymer surfaces are usually patterned and modified by lithography based plasma etching and deposition, coating on top of patterned substrates, and/or soft-lithography pattern transferring, and more recently creating stimuli-responsive surface cracking, wrinkling [9-13] and other deformation on smart material surfaces [14,15, 16].

FIB technique has proven its efficiency in micro/nano-engineering on semiconductor, metal or metal oxides with its unique capability for rapid prototyping and high precision [17,18]. The fundamental mechanism of FIB is that highly energetic ions driven by electrical field knock atoms off the material surface by electro-collision and recoil action between the ion and target material surface (Fig.1). For ion milled surfaces, the morphological evolution can cause the kinetic roughness which has attracted much research interest in the last few decades [19-21]. However, limited attempts have been reported on the topic of FIB processing on polymeric substrates since the charging effect from the insulated polymer matrix significantly reduces the FIB manufacture precision, and the

understanding on the morphological evolution for ion milled polymer surface remains yet to be fully explored [22-25]. Compared to other surface morphology modification techniques, the FIB method has the great potential for scalable patterning with both roughness level and geometry size range from 10s nm to 10s μm.

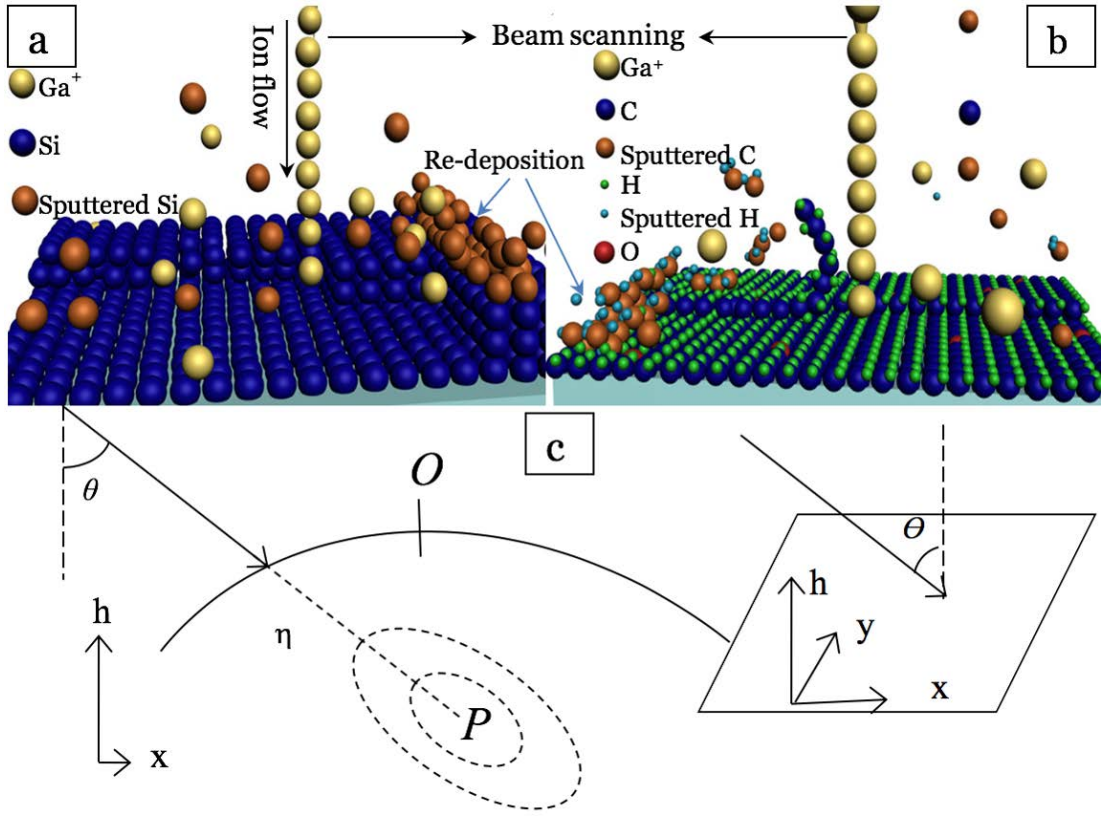

Figure 1. (color online) 3D schematics of FIB milling on (a) silicon; (b) conductive polymeric hybrids surface, (c) Following a straight trajectory (solid line) the ion penetrates an average distance a inside the solid (dash line) and completely releases its kinetic energy at *P*. The dotted equal energy contours indicate the energy decreasing area around point *P*. The energy released at point *P* contributes to erosion at *O*. The inset shows the laboratory coordinate frame: the ion beam forms an angle θ with the normal to the average surface orientation, z, and the in-plane direction x is chosen along the projection of the ion beam.

2. Theoretical background

As shown in Fig. 1, ion bombardment is commonly considered as atomic processes taking place inside the bombarded material within a finite penetration depth. The electrically manipulated ions pass through a distance *a* before they completely release their kinetic energy with a spatial distribution inside the target substrates. An ion releasing its energy at point P in the solid contributes energy to the surface point *O* that may induce the atoms in *O* to break their bonds and leave the surface or diffuse along it. The pattern formation by ion beam sputtering has been previously understood as the interplay between the unstable dependence of the sputtering yield on surface curvature and stabilizing surface relaxation mechanisms [26, 27]. The most successful model to predict surface evolution under ion sputtering was Bradley and Harper (BH) equation [28]. BH theory describes the ripple formation by discussing the surface topography $h(x, y, t)$, measured from an initial smooth configuration in the (x, y) plane. However, it could not explain the surface roughening well [29-31]. Therefore, Makeev, Barabási and Cuerno [32] refined the noisy Kuramoto-Sivashinsky (KS) equation [33, 34] based on the Sigmund theory of sputter erosion [35], where surface material was bombarded by ions, and included the Kardar-Parisi-Zhang (KPZ) nonlinear term to the BH equation. Cuerno et al [26, 36, 37] further developed an effective evolution equation:

$$\frac{\partial h}{\partial t} = -v\nabla^2 h + \lambda_1(\nabla h)^2 - \lambda_2\nabla^2(\nabla h)^2 - K\nabla^4 h, \quad (1)$$

where v, λ_1 and λ_2 are the average coefficients determined by the experimental parameters such as ion flux, ion energy, etc. For an amorphous solid in equilibrium with its vapor, the $K\nabla^4 h$ (known as MBE equation) [38] has been studied and obtained [39, 40]. Equation (1) was originally used to describe the dynamic scaling on the surface under the thermal surface diffusion, here, the conditional surface diffusion factor, K, can be decomposed with conductive induced PDE constant, D^c [39, 41]:

$$K = \frac{D^c \beta \Omega^2 M_{con}}{k_b T} \exp(\frac{-\Delta E}{k_b T}), \quad (2)$$

Where β is the surface free energy per unit, Ω represents the atomic volume, M_{con} denotes the number density of conductive particles, k_b is the Boltzmann constant, and T is the absolute temperature, ΔE is the activation energy for surface diffusion. The value of D^c could be determined by the evolved Nernst–Einstein equation [42, 43]:

$$D^c \equiv \frac{\sigma_{dc} k_b T}{e^2 M_{con}} \quad (3)$$

Here σ_{dc} represents the DC conductivity of sample, e is the elementary charge. To simplify the discussion, the symmetric case ($\delta = u$, which are the distribution distances in directions parallel and perpendicular along beam) was applied to current model, and the incident angle θ is zero. the linear wavelength instability could be calculated as [34]:

$$l_i = 2\pi\left(\frac{2K}{v}\right)^{1/2} \quad (4)$$

Which correlated to ion flux and matrix conductivity, and i refers to the direction (x *or* y). With small incidence angle $= -(F\alpha)/2\delta$, which is negative, and $F \equiv (\epsilon Jp/\sqrt{2\pi})\exp(-\frac{\alpha^2}{2\delta^2})$ [44, 45], where J means the average ion flux, ϵ denote the total energy carried by the ion and p is a proportionality constant between power deposition and rate of erosion. By considering the conductivity induced ion diffusion by Eq. (2) and (3), Eq. (1) could describe the surface roughening caused by PDE. The surface roughness evolution could be predicted form the following equation [26]:

$$\tau = v\lambda_2/(K\lambda_1) \quad (5)$$

Eq.(5) has been applied at different experimental conditions [46, 47].

We have recently demonstrated carbon-based polymer composites with exciting properties induced by the enhanced electrical conductivity [48, 49]. In this project, polymer composites with tunable electrical conductivities will be selected for comparative study of FIB induced polymer surface evolution. We describe an advanced FIB polymer surface patterning technology at micro/nano scale, enabled by overcoming the challenge from dielectric surface charging effect. A new concept of conductivity induced PDE is proposed to understand ion impacting on conductive polymer surface and predict the surface evolution during FIB. The ion bombarded surface topographic features with conductivity induced PDE are theoretically predicted using Monte Carlo simulation, and also experimentally assessed. The emerging application of fabricated surface is explored with surface wetting control. We expect that the findings in this work will advance the current understanding on the FIB fabrication on polymer surface.

3. Experimental methods

Conductive polymer nanocomposites such as polystyrene - carbon nano-particles (CNPs) were used to create the conductive polymer surfaces [50-53]. The styrene based precursor (PS, Veriflex®,

CRG Co. Ltd., US) [50, 51] and the CNPs (VULCAN® XC72R, CABOT, US), were ultrasonically agitated in a three neck flask for 2 hours at 1000 rpm [54]. Then the curing agent (Luperox ATC50, SIGMA) was added, and the mixture kept stirring for 45 min. Composite films with a thickness of 200 μm were made by casting the mixture into PTFE mold and baking in a vacuum oven at 75 °C for 36 hours.

The electrical conductivity was measured using an *I-V* testing set-up and thermo-electrical test was performed through a Schlumberger Solartron 1250 Frequency Response Analyser from 20 to 100 °C in an isolated chamber with an ambiance of air.

A dual-beam FIB instrument (FEI, Quanta3D FEG) equipped with liquid gallium ion source (Ga+, 30KeV) was used. Scanning electron microscopy (SEM, FEI Quanta3D FEG) was used to observe the microstructure. The topographic surface was assessed with an atom force microscopy (AFM, Triboscope, Hysitron Inc., US). Sputter yield was calculated through Monte Carlo simulation (TRIDYN, binary collision approximation ion irradiation simulation) [55, 56], which simulates the ion irradiation of amorphous targets in the binary collision approximation. It allows for a dynamic rearrangement of the local composition of the target material [57]. Therefore, effects in high-fluence implantation, ion mixing, and preferential sputtering caused by atomic collision processes can be concluded [58]. Considering the current macromolecular based hybrids system, an enthalpy of sublimation value (6.2 eV) was set in simulation with consulting the chemically covalent bond energies and atom composition.

4. Results and discussion

Figure 2a shows the surface of conductive nanocomposite, it can be clearly evidenced that the CNPs distributed uniformly throughout the textured polymer matrix. Fig. 2b presents the DC conductivity as a function of CNP concentrations at room temperature. When CNP concentrations (φ_{CNP}) increased from 0.5 to 2 vol.%, the conductivity dramatically increased from 1×10^{-8} to 100 S/m, and this increment slowed down when the CNP concentration exceeded 2 vol.%. The conductivity for φ_{CNP} > 2 vol.% was sufficient to enter the general semiconductor region. Such percolation system with random conductor and insulator mixtures has been well understood as a polymer-based inorganic (σ_1) – organic (σ_2, $\sigma_2 << \sigma_1$) conducting system, or resistors and capacitors [59-61]. At a lower CNP concentration, conduction is mainly dominated by hopping conduction among the nanofillers, thus appeared closer to the insulator [59, 61]. They became conductors when the filler concentration increased to a critical value, i.e., the percolation threshold (φ_c), which formed the electron bridge within the substrate by the filler state [62]. To determine φ_c, the conductivity σ was fitted based on the power laws [59, 63]:

$$\sigma(\varphi_{CNP}) \propto (\varphi_c - \varphi_{CNP})^{-s} \quad \text{when } \varphi_{CNP} < \varphi_c \tag{6}$$

$$\sigma(\varphi_{CNP}) \propto (\varphi_{CNP} - \varphi_c)^{t} \quad \text{when } \varphi_{CNP} > \varphi_c \tag{7}$$

Where t and s are the critical exponents in the conducting region and insulating region. The linear-fitting results clearly defined the threshold network with $\varphi_c = 2$ *vol.%*, $t = 0.858$, and $s = 4.75$ (the inset in Fig. 2b). Previous reports [64, 65] addressed that a higher critical value ($t > 2$) in polymer/CNP system will reduce the conductive efficiency. Whereas, good conductive efficiency ($t = 0.858$) was achieved in this work, which attributes to the uniform nanofillers distribution by the adopted techniques.

The conductivity-temperature relation was shown in Fig. 2c. The measured conductivity gradually increased with the rising temperature which enhanced the hopping conductivity in composites [66]. The sample conductivity for 2 vol.% CNP/PS approached the percolation limit of an insulator-dominating state, and further rises in temperature significantly increased the conductivity through the enhanced hopping. When the CNP content was above φ_c, the CNP particles/clusters were more likely to link with each other, forming a continuously distributed CNP network in the matrix. Fig. 2d summarizes the calculated conductivity diffusion coefficients with dependency on temperature. For the composites which hadn't formed the threshold network, the diffusion coefficients were low, and the value located in the ion diffusion range inside of insulated solid (<10^{-18} m^2/sec) [67]. With the CNP

content increased, the PDE constant significantly increased from 10^{-21} to 10^{-11}. It should be noticed that the diffusion constant for ion-liquid system is 10^{-11}~10^{-9} m²/sec [67]. This giant change was caused by conductive network generation with adding CNP, which enhanced the ion diffusion capability dramatically. With the information in Fig. 2c-d, the thermal effect on sample conductivity or D^c, which caused a changing factor of 10-100, is negligible when comparing the giant improvement by increasing conductivity.

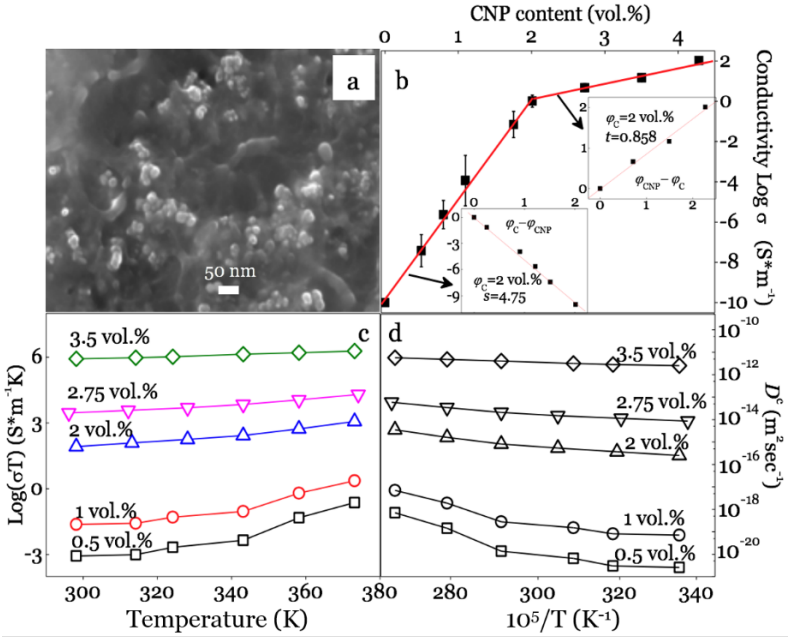

Figure 2. (color online) (a), SEM observation of the conductive surface of 2 vol% CNP/PS; (b), DC conductivity results as a function of CNP content, the inlets linear fitting curves needed for determining the threshold value; (c) DC conductivity for composites with dependency on temperature and CNP concentration, (d) Calculated conductivity diffusion coefficients as a function of temperature.

As it has been introduced, all coefficients in Eq. (1) are determined by ion flux and K. The coefficient K could be calculated with the D^c (in Fig.2d) by Eq. (2) and Eq.(3). it is now straightforward to obtain all values under the flux condition. Since the main goal of this work was to investigate the influence from material, the study started with a fixed ion flux $\Phi = 1.2 \times 10^9$ *ions/(μm²sec)*. With the Monte Carlo algorithm, there could be obtained that, $v = 187$ *nm²/min*, $\lambda_1 = 78.4$ *nm/min*, $\lambda_2 = 4373.2$ *nm³/min*. The simulated roughness τ was displayed in Fig. 3a-c, comparing with the experimental AFM plots. The quantitative agreement in the order of magnitude between the experimental and the theoretical results was found for predicting the surface evolution trend, the surface roughness decreased constantly with the CNP content increased in composites. The experimental values were only half of theoretical ones for 1 vol.% and 2 vol.% CNP/PS composites. For 3.5 vol.% CNP/PS, the magnitude of the experimental result agreed well with theory, which could be attributed to the metallic type surface morphological evolution happening during ion processing caused by the high sample conductivity. Furthermore, the asymptotic morphologies revealed the increasing l_i values as well as the reduction of τ with the target conductivity increases, where implying a higher self-smoothing effect and a thermal relaxation mechanism led to and a less defined pattern order for the composites hybrid. The observed discrepancy between the experimental data and theoretical prediction may be explained by ignoring the rapid temperature increases during ion sputter which could induce the thermal diffusion.

The milling depth values were plotted as a function of ion flux in Fig.3d-f, the grey areas represented the total removal depth including the targeted milling depth (500 nm) and the calculated roughness, while the up-edge indicated the accumulating value of roughness and targeted removal depth. As predicted, the self-smoothing conductive induced PDE were found as shown in each figure. Both the experimental and numerical morphologies presented a low surface roughness associated with

low ion flux values in contrary to the much higher roughness values under higher ion flux. This could be derived from the flux related parameters in Eq.(5), v, λ_1 and λ_2 , which change significantly with applying higher ion flux. Moreover, the experimental average removal depth reduced at high ion flux for all samples, this could be due to the inaccurate numerical calculation at high roughnesses.

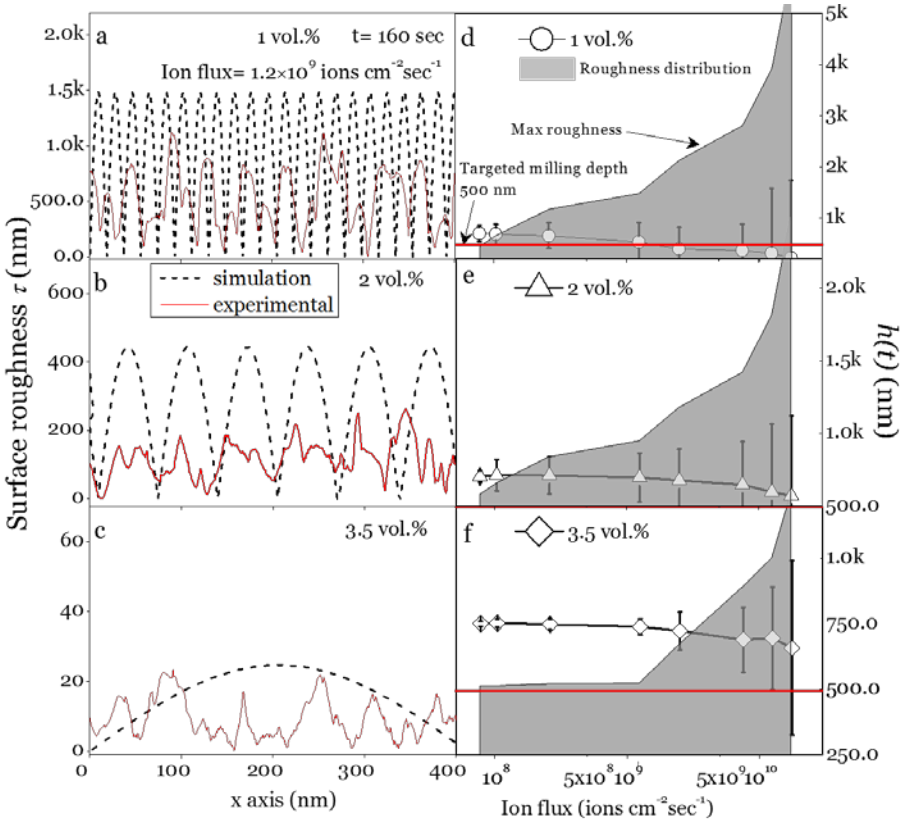

Figure 3. (color online) a-c. Experimental AFM profiles on ion milled surface and numerical longitudinal plots for different composites (milling time=160 sec); d-f. Time evolving milling efficiency (removal depth, h(t)) with surface roughness (error bar), the gray area represent the roughness with targeted removal depth of 500 nm.

Fig. 3d-f shows the roughness reduced with increased conductivity both in experimental and numerical results, proving that the pattern characteristics are dominated by the sample conductive. Fig. 3a-c also reflected that roughness peak at high conductivity values is broader when sample was bombarded at same flux values. It should be addressed that, the ion flux employed in this work is 10-1000 times higher than those have been reported [26, 36, 68], the thermally activated surface diffusion effect couldn't be ignored when the target's temperature increases, which will bring the self-smoothing effect on the ion bombed surface as well as conductivity induced PDE do.

The experimental topographic information was summarized in Fig.4 with SEM images, AFM profiles and statistical analysis for AFM data. The deteriorating trends were presented with dependencies to ion flux and sample conductivity, the SEM observation illustrates that higher ion flux bring lager surface roughness more than better removal efficiency, probably combined with the re-deposition [69]. The milling precision was improved with sample conductivity increases, which could be identified from the evolving morphology in SEM images under different ion flux, simultaneously, the AFM contour plots agree this improvement well with showing concentrated milled depth. The contour plots also reflect that the highest roughness appears for 1 vol.% CNP/PS which indicates milling accuracy was lowered with low conductivity. The statistical analysis from AFM suggests that the milling depth distributed in a board range for 1 vol.% sample especially under the high ion flux (1.25×10^{10} and 1.75×10^{10} ions/(μm²sec)). Meanwhile, a concentrated distribution for 3.5 vol.% CNP/PS was observed under the low ion flux which represented high uniformity for the milling depth. Fig.4 also

reveals that the actual average milling depths were around 700 nm for most conditions with considerable errors, which is a little bit far away from the target removal depth of 500 nm. The possible reason could be the thermal induced polymer chain broken during the high energy ion sputter process, which could be understand as thermal induced positive effect. Although the improved milling precision had been achieved for 2 vol.% and 3.5 vol.% CNP/PS, the actual milling depth decreases for 1 vol.% CNP/PS when ion flux increased. This could resort to the calculation uncertainty caused by the ultimately roughness as previous mentioned, the residual surface charge and the re-deposition caused by molecular chain breaking [70]. Additionally, the Monte Carlo codes in this work considered the effects in high-fluence implantation, ion mixing and preferential sputtering caused by atomic collision processes, and proved a positive correspondence between ion milling efficiency and sample conductivity, but it didn't count the thermal induce surface diffusion which has been previously proved with stabilization effect on ion-bombing surface [26, 44, 71].

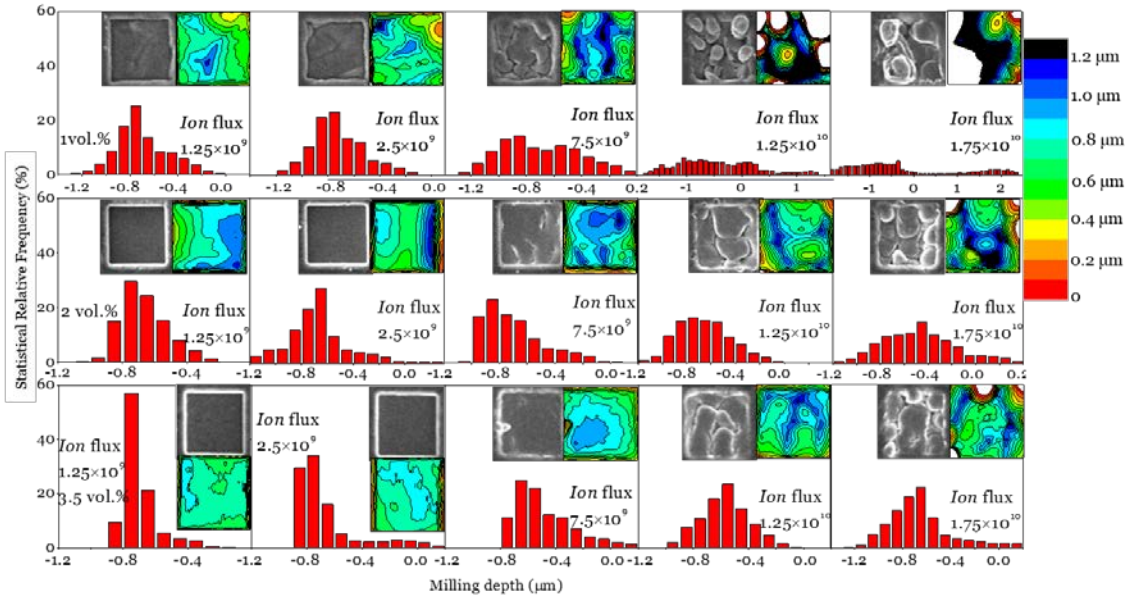

Figure 4. Statistical depth distribution analysis for the milled square patterns (5×5 μm2, milling time is 160 sec) based on AFM results (see inlet, contour plots) under different ion flux, combined with the SEM images (in inlet).

5. Application demonstration

The CNPs-PS polymer matrix surfaces were FIB ion milled into different micro-roughness regions (2 × 2 mm² areas pre-patterned with 20 × 20 μm² square pattern arrays) with milling depths range from 0.5 to 1.2 μm, and R_a (arithmetic mean roughness) values range from 700 to 4800 nm (0.7 to 4.8 μm). Different patterns are demonstrated in Fig 5a, from line array to dedicated probe shape. The processing efficiency and the precision are significantly increased. We next selected the dot array pattern (FIG S1) for the surface wetting testing. A self-assembly monolayer (SAM) of Trichloro(1H,1H,2H,2H-perfluorooctyl)silane (FOTS, Sigma-Aldrich), was applied from the vapor phase at room temperature (~20 °C) for 30 min to facilitate a conformal hydrophobic layer over the CNPs-PS topologies.

To set a benchmark, the static contact angle (CA) of a 2μL Deionized (DI) water on smooth FOTS surface was measured to be 107°. Fig. 5b shows that on the modified CNPs-PS surface, the CA ranges from (contact angles CA range from 108.3° to 150.8°, Fig.5c). Dynamic CA measurements (advancing and receding) have also been performed, with different CA hysteresis (Fig.5d) values range from 31.4° to 8.3°. These values shown in Fig.5c-5d were close to Wenzel state prediction at lower roughness (< 3.5 μm), and closer to Cassie-Baxter state at higher roughness [13] with $CA = 150.8°$ and $CAH = 8.3°$, which meets the superhydrophobic surfaces (SHS) criteria – $CA > 150°$ and $CAH < 10°$.

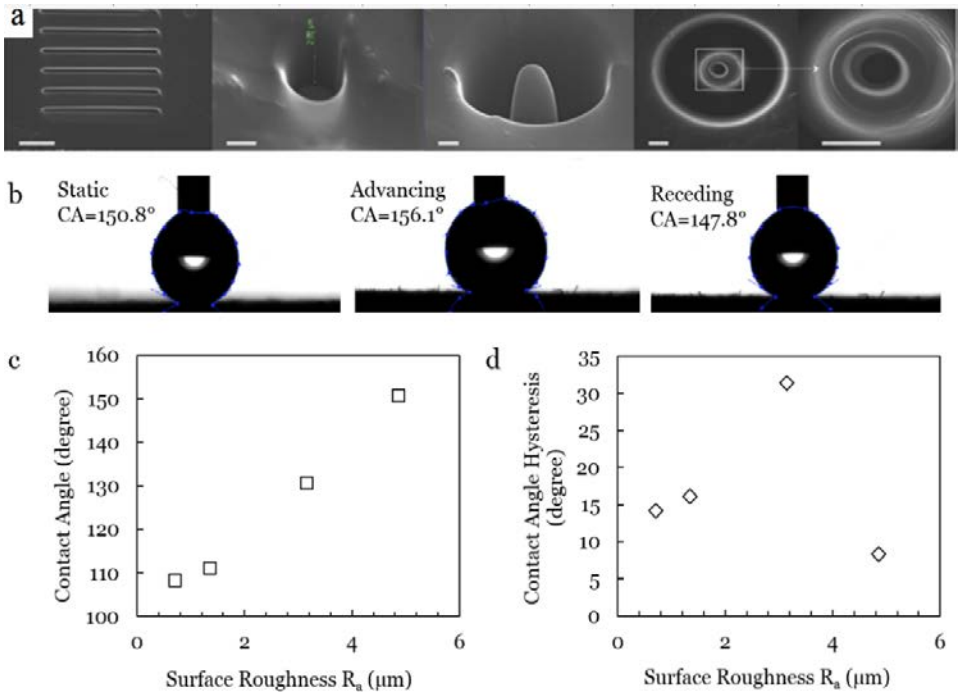

Figure 5. (a) FIB engineered nanostructures, from left to right, lines pattern, nano-hole, nano-probe, nano-tunnel, the scale bar is 500 nm; Static contact angle (CA) and contact angle hysteresis (CAH = advancing CA - receding CA) characterisation on patterned CNPs-PS polymer with FOTS layer: (b) CA and CAH values of a DI droplet on superhydrophobic surface (Ra=4.8 μm); and relationships between (c) static contact angles and surface roughnesses; (d) contact angle hysteresis and surface roughnesses.

6. Conclusion

Good structure-properties relations were revealed with the homogeneous dispersing state of CNPs in PS matrix from SEM observation, the measured conductivity and the stable electrical-temperature performance. The assessment on ion milled surface indicates that the milling accuracy and surface roughness are highly dependent on the sample's conductivity. A good agreement between experimental results and the theoretical prediction is achieved on describing the surface evolving trend, including the general analytical conditions for the coarsening process to occur and the roughness of the surface with the different ion flux and material conductivity. Resulting micro-roughness patterns were coated with hydrophobic monolayer FOTS and demonstrated surface wettability control resulting in hydrophobic and superhydrophobic surfaces (contact angles CA range from 108.3° to 150.8°) with different CA hysteresis values range from 31.4° to 8.3°.

It must be noted that the ion bombardment on macromolecular system is far more complicated than the silicon one, it would be very interesting to look into the ion sputtering on conductive polymer (composites) surface's with conductivity and thermal induced PDEs, and more substrate related factors such as the molecular chain movements, polymer degradation, etc., in the future work.

Supplementary Materials: The following are available online at www.mdpi.com/xxx/s1, Figure S1: title, Table S1: title, Video S1: title.

Author Contributions: For research articles with several authors, a short paragraph specifying their individual contributions must be provided. The following statements should be used "conceptualization, X.X. and Y.Y.; methodology, X.X.; software, X.X.; validation, X.X., Y.Y. and Z.Z.; formal analysis, X.X.; investigation, X.X.; resources, X.X.; data curation, X.X.; writing—original draft preparation, X.X.; writing—review and editing, X.X.; visualization, X.X.; supervision, X.X.; project administration, X.X.; funding acquisition, Y.Y.", please turn to the CRediT taxonomy for the term explanation. Authorship must be limited to those who have contributed substantially to the work reported.

Funding: This research was funded by EPSRC (Grant Nos. EP/N007921/1 and EP/L026899/1).

Acknowledgments: The authors would like to thank Everbeing who donated the probing system used in this work, and MEMSstar, Ltd., for providing the SAM coating facility. Data associated with this paper are available via Northumbria Research Data Management scheme.

Conflicts of Interest: Declare conflicts of interest or state "The authors declare no conflict of interest." Authors must identify and declare any personal circumstances or interest that may be perceived as inappropriately influencing the representation or interpretation of reported research results. Any role of the funders in the design of the study; in the collection, analyses or interpretation of data; in the writing of the manuscript, or in the decision to publish the results must be declared in this section. If there is no role, please state "The funders had no role in the design of the study; in the collection, analyses, or interpretation of data; in the writing of the manuscript, or in the decision to publish the results".

Appendix A

The appendix is an optional section that can contain details and data supplemental to the main text. For example, explanations of experimental details that would disrupt the flow of the main text, but nonetheless remain crucial to understanding and reproducing the research shown; figures of replicates for experiments of which representative data is shown in the main text can be added here if brief, or as Supplementary data. Mathematical proofs of results not central to the paper can be added as an appendix.

Appendix B

All appendix sections must be cited in the main text. In the appendixes, Figures, Tables, etc. should be labeled starting with 'A', e.g., Figure A1, Figure A2, etc.

References

1. J. T. Simpson, S. R. Hunter and T. Aytug, Superhydrophobic materials and coatings: a review, *Rep. Prog. Phys*., **2015**, *78*, 086501.
2. E. Yilgor, C. K. Soz, and Iskender Yilgor, Wetting behavior of superhydrophobic poly (methyl methacrylate), *Prog. in Organic Coatings*, **2018,** *125*, 530-536.
3. B. Bhushan and Y.C. Jung, Natural and biomimetic artificial surfaces for superhydrophobicity, self-cleaning, low adhesion, and drag reduction, *Prog. Mater. Sci.*, **2011,** *56*, 1-108.
4. S. Wang, K. Liu, X. Yao and L. Jiang, Bioinspired surfaces with superwettability: new insight on theory, design, and applications, *Chem. Rev.*, **2015,** *115*, 8230-8293.
5. V. Kochkodan and N. Hilal, A comprehensive review on surface modified polymer membranes for biofouling mitigation, *Desalination*, **2015,** *356*, 187-207.
6. M. J. Kreder, J. Alvarenga, P. Kim and J. Aizenberg, Design of anti-icing surfaces: smooth, textured or slippery, *Nature Reviews Materials*, **2016,** *1*, 15003.
7. C. Zhang, D. A. Mcadams II, J. C. Grunlan, Nano/micro-manufacturing of bioinspired materials: A review of methods to mimic natural structures, *Advanced Materials*, **2016,** *28*, 6292-6321.
8. P. Zhang, L. Lin, D. Zang, X. Guo and M. Liu, Designing Bioinspired Anti-Biofouling Surfaces based on a Superwettability Strategy, *Small*, **2017,** *13*, 1503334.
9. D. Wang, N. Cheewaruangroj, Y. Li, G. McHale, Y. Jiang, D. Wood, J.S. Biggins and B. B. Xu, Spatially configuring wrinkle pattern and multiscale surface evolution with structural confinement, *Advanced Functional Materials,* **2018,** *28,* 1704228.
10. X. Huang, Y. Sun and S. Soh, Stimuli-responsive surfaces for tunable and reversible control of wettability, *Advanced Materials,* **2015,** *27,* 4062-4068.
11. D. Rhee, W. K. Lee and T. W. Odom, Crack-Free, Soft Wrinkles Enable Switchable Anisotropic Wetting, *Angew. Chem. Int. Ed.,* **2017,** *56,* 6523-6527.
12. H. Lu, Y. Liu, B. B. Xu, D. Hui and Y.Q. Fu, Spontaneous biaxial pattern generation and autonomous wetting switching on the surface of gold/shape memory polystyrene bilayer, *Composites Part B: Engineering,* **2017,** *122*, 9-15.
13. Y. Liu, J. Genzer and M.D. Dickey, "2D or not 2D": Shape-programming polymer sheets, *Progress in Polymer Science,* **2016,** *52*, 79-106.
14. B. Xu, W. M. Huang, Y. T. Pei, Z. G. Chen, A. Kraft, R. Reuben, J.T.M. De Hosson and Y.Q. Fu, Mechanical properties of attapulgite clay reinforced polyurethane shape-memory nanocomposites, *European Polymer Journal,* **2009,** *45*, 1904-1911.
15. M-W. Moon, S. H. Lee, J-Y. Sun, K. H. Oh, A. Vaziri, and J. W. Hutchinson, Wrinkled hard skins on polymers created by focused ion beam, *PNAS*, **2007**, 104, 1130-1133.
16. B. Xu, Y. Q. Fu, W. M. Huang, Y. T. Pei, Z. G. Chen, J.T.M. De Hosson, A. Kraft and R.L. Reuben, Thermal-mechanical properties of polyurethane-clay shape memory polymer nanocomposites, *Polymers,* **2010,** *2*, 31-39.
17. L. A. Giannuzzi, and M. Utlaut, A review of Ga+ FIB/SIMS, *Surf. Interface. Anal.,* **2011,** *43,* 475,
18. P. Roediger, H. D. Wanzenboeck, S. Waid, G. Hochleitner, and E. Bertagnolli, Focused-ion-beam-inflicted surface amorphization and gallium implantation—new insights and removal by focused-electron-beam-induced etching, *Nanotechnology,* **2011,** *22,* 235302.
19. J. Vollner, B. Ziberi, F. Frost, and B. Rauschenbach, Topography evolution mechanism on fused silica during low-energy ion beam sputtering, **2011,** *J. Appl. Phys. 109*, 043501.
20. G. S. Oehrlein, R. J. Phaneuf, and D. B. Graves, Plasma-polymer interactions: A review of progress in understanding polymer resist mask durability during plasma etching for nanoscale fabrication, *J. Vac. Sci. Technol. B,* **2011,** *29*, 010801.
21. D. G. Cahill, Morphological instabilities in thin-film growth and etching, *J. of Vacuum Science & Technology A: Vacuum, Surfaces, and Films,* **2003,** *21,* S110.

22. W. Brostow, B. P. Gorman, and O. Olea-Mejia, Focused ion beam milling and scanning electron microscopy characterization of polymer+ metal hybrids, *Mater. Lett.,* **2007,** *61,* 1333.
23. S. Brunner, P. Gasser, H. Simmler, and K. Ghazi Wakili, Investigation of multilayered aluminium-coated polymer laminates by focused ion beam (FIB) etching, *Surf. Coat. Tech.,* **2006,** *200,* 5908,
24. E. Pialat, T. Trigaud, V. Bernical, and J. P. Moliton, Milling of polymeric photonic crystals by focused ion beam, *Mat. Sci. Eng.: C.,* **2005,** *25,* 618.
25. J. J. L. Mulders, D. A. M. de Winter, and W. J. H. C. P. Duinkerken, Measurements and calculations of FIB milling yield of bulk metals, *Microelectron. Eng.,* **2007,** *84,* 1540.
26. J. Muñoz-García, R. Gago, L. Vázquez, J. Angel Sánchez-García, and R. Cuerno, Observation and Modeling of Interrupted Pattern Coarsening: Surface Nanostructuring by Ion Erosion, *Phys. Rev. Lett.,* **2010,** *104,* 026101.
27. J. Muñoz-García, M. Castro, and R. Cuerno, Nonlinear Ripple Dynamics on Amorphous Surfaces Patterned by Ion Beam Sputtering, *Phys. Rev. Lett.,* **2006,** *96,* 086101.
28. R. M. Bradley, and J. M. E. Harper, Theory of ripple topography induced by ion bombardment, *Journal of Vacuum Science & Technology A: Vacuum, Surfaces, and Films,* **1988,** *6,* 2390.
29. E. A. Eklund, R. Bruinsma, J. Rudnick, and R. S. Williams, Submicron-scale surface roughening induced by ion bombardment, *Phys. Rev. Lett.,* **1991,** *67,* 1759.
30. T. Mitsui, D. Stein, Y.-R. Kim, D. Hoogerheide, and J. A. Golovchenko, Nanoscale volcanoes: accretion of matter at ion-sculpted nanopores, *Phys. Rev. Lett.,* **2006,** *96,* 036102.
31. J. Rodriguez-Laguna, S. N. Santalla, and R. Cuerno, Intrinsic geometry approach to surface kinetic roughening, *Journal of Statistical Mechanics-Theory and Experiment,* **2011,** *2011,* P05032.
32. M. Kardar, G. Parisi, and Y.-C. Zhang, Dynamic scaling of growing interfaces, *Phys. Rev. Lett.,* **1986,** *56,* 889.
33. M. A. Makeev, and A.-L. Barabasi, Effect of surface roughness on the secondary ion yield in ion sputtering, *Appl. Phys. Lett.,* **1998,** *73,* 1445,
34. R. Cuerno, and A.-L. Barabási, Dynamic scaling of ion-sputtered surfaces, *Phys. Rev. Lett.,* **1995,** *74,* 4746,
35. P. Sigmund, Theory of sputtering. I. Sputtering yield of amorphous and polycrystalline targets, *Physical Review,* **1969,** *184,* 383.
36. M. Castro, R. Cuerno, L. Vázquez, and R. Gago, Self-organized ordering of nanostructures produced by ion-beam sputtering, *Phys. Rev. Lett.,* **2005,** *94,* 016102.
37. J. Muñoz-García, R. Cuerno, and M. Castro, Coupling of morphology to surface transport in ion-beam-irradiated surfaces: normal incidence and rotating targets, *J. Phys.: Condens. Mat.,* **2009,** *21,* 224020.
38. T. Walmann, A. Malthe-Sørenssen, J. Feder, T. Jøssang, P. Meakin, and H. H. Hardy, Scaling relations for the lengths and widths of fractures, *Phys. Rev. Lett.,* **1996,** *77,* 5393.
39. W. W. Mullins, Theory of thermal grooving, *J. Appl. Phys.,* **1957,** *28,* 333.
40. C. Herring, Effect of Change of Scale on Sintering Phenomena, *J. Appl. Phys.,* **1950,** *21,* 301.
41. J. F. Mullins, and M. F. Lettieri, Chemosurgery of facial wrinkles, *Texas state journal of medicine,* **1963,** *59,* 488.
42. H. Jain, and J. N. Mundy, Analysis of ac conductivity of glasses by a power law relationship, *J. Non-cryst. Solids.,* **1987,** *91,* 315.
43. S. Voss, A. W. Imre, and H. Mehrer, Mixed-alkali effect in Na–Rb borate glasses: A tracer diffusion and electrical conductivity study, *Phys. Chem. Chem. Phys.,* **2004,** *6,* 3669.
44. M. A. Makeev, R. Cuerno, and A.-L. Barabási, Morphology of ion-sputtered surfaces, *Nuclear Instru. and Meth. in Phys. Res. Sect. B: Beam Inter. with Mater. and Atoms,* **2002 ,** *197,* 185.
45. M. A. Makeev, and A.-L. Barabasi, Secondary ion yield changes on rippled interfaces, *Appl. Phys. Lett.,* **1998,** *72,* 906.
46. J. Muñoz-García, M. Castro, and R. Cuerno, Nonlinear ripple dynamics on amorphous surfaces patterned by ion beam sputtering, *Phys. Rev. Lett.,* **2006,** *96,* 086101,
47. J. H. Kim, N. B. Ha, J. S. Kim, M. Joe, K. R. Lee, and R. Cuerno, One-dimensional pattern of Au nanodots by ion-beam sputtering: formation and mechanism, *Nanotechnology,* **2011,** *22,* 285301.
48. H. Lu, X. Wang, Y. Yao, J. Gou, D. Hui, B. Xu, Y.Q. Fu, Synergistic effect of siloxane modified aluminum nanopowders and carbon fiber on electrothermal efficiency of polymeric shape memory nanocomposite, *Composites Part B: Engineering,* **2015,** *80,* 1-6.
49. X. Dai, Y. Du, J. Yang, D. Wang, J. Gu, Y. Li, S. Wang, B.B. Xu and J. Kong, Recoverable and self-healing electromagnetic wave absorbing nanocomposites, *Composites Science and Technology,* **2019,** *174,* 27-32.

50. P. J. Hood, and D. E. Havens, edited by U. S. PatentUS, **2006**, p. 12.
51. P. J. Hood, S. Garrigan, and F. Auffinger, edited by U. S. PatentUS, **2007**, p. 18.
52. B. Xu, L. Zhang, Y.T. Pei, J.K. Luom S.W. Tao, J.T.M. De Hosson, Y.Q. Fu, Electro-responsive polystyrene shape memory polymer nanocomposites, *Nanosci. Nanotech. Lett.,* **2012,** *4,* 814-820.
53. M. Lei, B. Xu, Y.T. Pei, H. B. Lv and Y. Q. Fu, Micro-mechanics of nanostructured carbon/shape memory polymer hybrid thin film, *Soft Matter,* **2016,** *12*, 106-114.
54. B. Xu, Y. Q. Fu, M. Ahmad, J. K. Luo, W. M. Huang, A. Kraft, R. Reuben, Y. T. Pei, Z. G. Chen and J. T. M. De Hosson, Thermo-mechanical properties of polystyrene-based shape memory nanocomposites, *J. Mater. Chem.,* **2010,** *20,* 3442.
55. A. Barna, L. Kotis, J. L. Labar, Z. Osvath, A. L. Toth, M. Menyhard, A. Zalar and P. Panjan, Producing metastable nanophase with sharp interface by means of focused ion beam irradiation, *J. Appl. Phys.,* **2007,** *102,* 044305.
56. M. L. Roush, T. D. Andreadis, F. Davarya, and O. F. Goktepe, Dynamic simulation of changes in near-surface composition during ion bombardment, *Appl. Surf. Sci.,* **1982,** *11-2,* 235.
57. W. Möller, W. Eckstein, and J. P. Biersack, Tridyn-binary collision simulation of atomic collisions and dynamic composition changes in solids, *Comput. Phys. Commun.,* **1988,** *51,* 355.
58. J. Sun, X. Luo, J. M. Ritchie, W. Chang, and W. Wang, An investigation of redeposition effect for deterministic fabrication of nanodots by focused ion beam, *Precis. Eng.,* **2012,** *36,* 31.
59. Z. M. Dang, Y. H. Lin, and C. W. Nan, Novel ferroelectric polymer composites with high dielectric constants, *Adv. Mater.,* **2003,** *15*, 1625.
60. C. Pecharroman, F. Esteban-Betegon, J. F. Bartolome, S. Lopez-Esteban and J. S. Moya, New Percolative $BaTiO_3$–Ni Composites with a High and Frequency-Independent Dielectric Constant, *Adv. Mater.,* **2001,** *13,* 1541.
61. P. Pöschke, S. M. Dudkin, I. Alig, Dielectric spectroscopy on melt processed polycarbonate—multiwalled carbon nanotube composites, *Polymer,* **2003,** *44,* 5023.
62. O. Regev, P.N.B. ElKati, J. Loos, C.E. Koning, Preparation of Conductive Nanotube–Polymer Composites Using Latex Technology, *Adv. Mater.,* **2004,** *16,* 284.
63. Z. M. Dang, L. Wang, Y. Yin, Q. Zhang, and Q. Q. Lei, Giant dielectric permittivities in functionalized carbon-nanotube/electroactive-polymer nanocomposites, *Adv. Mater.,* **2007,** *19,* 852.
64. M. Kolb, R. Botet, and R. Jullien, Scaling of Kinetically Growing Clusters, *Phys. Rev. Lett.,* **1983,** *51,* 1123.
65. B. M. L Karásek, S Asai, M Sumita, Percolation concept: polymer-filler gel formation, electrical conductivity and dynamic electrical properties of carbon-black-filled rubbers, *Polym. J.,* **1996,** *28,* 121.
66. A. K. Jonscher, New interpretation of dielectric loss peaks, *Nature,* **1975,** *253,* 717.
67. H. Mehrer, in Springer Ser. Solid-State Sci., edited by H. Mehrer (Springe, 2007), p. 221.
68. M. Nicoli, R. Cuerno, and M. Castro, Unstable nonlocal interface dynamics, *Phys. Rev. Lett.,* **2009,** *102,* 256102.
69. T. Ishitani, T. Ohnishi, Y. Madokoro, and Y. Kawanami, Focused-ion-beam ''cutter''and ''attacher''for micromachining and device transplantation, *J. Vac. Sci. Technol. B,* **1991,** *9,* 2633.
70. X. Roy, P. Sarazin, and B. D. Favis, Ultraporous nanosheath materials by layer-by-layer deposition onto co-continuous polymer-blend templates, *Adv. Mater.,* **2006,** *18,* 1015.
71. R. Cuerno, L. Vazquez, R. Gago, and M. Castro, Surface nanopatterns induced by ion-beam sputtering, *J. Phys.: Condens. Mat.,* **2009,** *21,* 220301.